NSRRC-J05181(2016)

Materials Views
www.MaterialsViews.com

ADVANCED FUNCTIONAL MATERIALS
www.afm-journal.de

FULL PAPER

Donor–Acceptor Poly(3-hexylthiophene)-*block*-Pendent Poly(isoindigo) with Dual Roles of Charge Transporting and Storage Layer for High-Performance Transistor-Type Memory Applications

Jau-Tzeng Wang, Shoichi Takashima, Hung-Chin Wu, Yu-Cheng Chiu, Yougen Chen, Takuya Isono, Toyoji Kakuchi, Toshifumi Satoh, and Wen-Chang Chen**

Field-effect transistor memories usually require one additional charge storage layer between the gate contact and organic semiconductor channel. To avoid such complication, new donor–acceptor rod–coil diblock copolymers (P3HT$_{44}$-*b*-Piso$_n$) of poly(3-hexylthiophene) (P3HT)-*block*-poly(pendent isoindigo) (Piso) are designed, which exhibit high performance transistor memory characteristics without additional charge storage layer. The P3HT and Piso blocks are acted as the charge transporting and storage elements, respectively. The prepared P3HT$_{44}$-*b*-Piso$_n$ can be self-assembled into fibrillar-like nanostructures after the thermal annealing process, confirmed by atomic force microscopy and grazing-incidence X-ray diffraction. The lowest-unoccupied molecular orbital levels of the studied polymers are significantly lowered as the block length of Piso increases, leading to a stronger electron affinity as well as charge storage capability. The field-effect transistors (FETs) fabricated from P3HT$_{44}$-*b*-Piso$_n$ possess p-type mobilities up to 4.56×10^{-2} cm^2 V^{-1} s^{-1}, similar to that of the regioregular P3HT. More interestingly, the FET memory devices fabricated from P3HT$_{44}$-*b*-Piso$_n$ exhibit a memory window ranging from 26 to 79 V by manipulating the block length of Piso, and showed stable long-term data endurance. The results suggest that the FET characteristics and data storage capability can be effectively tuned simultaneously through donor/acceptor ratio and thin film morphology in the block copolymer system.

1. Introduction

Polymeric semiconductors have attracted extensive research efforts as active materials in optoelectronic devices, such as organic field-effect transistors (OFETs), solar cells, and electrical memories, due to their superior solution processability, thin film flexibility, and tunable electronic properties.[1–5] More recently, they have been introduced in memory devices based on a conventional transistor architecture (called transistor-type memory device), which possess the advantages of nondestructive readout with a multibit data storage and simple device integration.[6–8] Compared to the conventional FET, transistor-type memory devices require an additional distinct layer for charge trapping as well as digital information storage. Three main design strategies, including ferroelectric materials,[9] polymer electrets,[10–16] and floating gate dielectrics,[17–22] for a charge storage layer between semiconducting active layer and gate contact are explored.However, the currently reported transistor-type memories that require an additional charge storage layer might enable complicated processing steps. It would be of significant advantages to develop organic materials with both charge transporting and charge storage characteristics for OFET memory devices.

Conjugated moieties based donor (D)–acceptor (A) block copolymers that possess distinguishing features of combining nanostructure formation and electronic/optoelectronic properties could be an ideal candidate for OFET memory devices, with both charge transporting and charge storage characteristics. Poly(3-hexylthiophene) (P3HT) as rod segment in block copolymers[23–27] provided the advantages of not only appropriate charge carrier mobility but also versatile synthetic approaches. Block copolymers consisting of P3HT coupled with electron-withdrawing coil segments, such as C_{60},[28,29] perylene bisimide,[23,25] and oxadiazole,[30] were prepared via atom transfer radical polymerization (ATRP),[31,32] anionic polymerization,[33,34] or click reaction.[35,36] The thin film morphologies and electrical properties of these P3HT-based D–A block copolymers,

J.-T. Wang, Dr. H.-C. Wu, Dr. Y.-C. Chiu, Prof. W.-C. Chen
Department of Chemical Engineering
National Taiwan University
Taipei 10617, Taiwan
E-mail: chenwc@ntu.edu.tw
S. Takashima
Graduate School of Chemical Sciences and Engineering
Hokkaido University
Sapporo 060-8628, Japan
Dr. Y. Chen, Dr. T. Isono, Prof. T. Satoh, Prof. T. Kakuchi
Faculty of Engineering
Hokkaido University
Sapporo 060-8628, Japan
E-mail: satoh@poly-bm.eng.hokudai.ac.jp

DOI: 10.1002/adfm.201504957

© 2016 WILEY-VCH Verlag GmbH & Co. KGaA, Weinheim

ADVANCED FUNCTIONAL MATERIALS
www.afm-journal.de

Materials Views
www.MaterialsViews.com

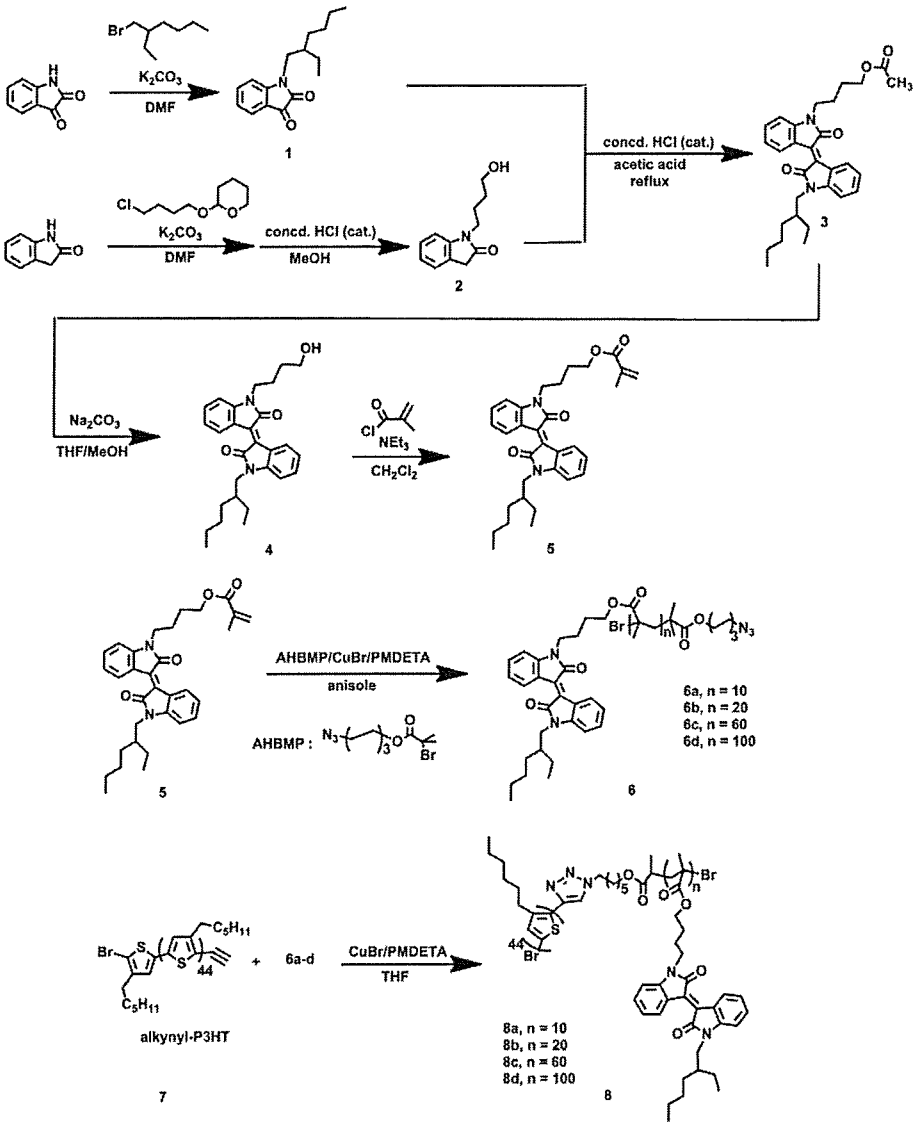

Scheme 1. Synthesis of $P3HT_{44}$-*b*-$Piso_n$ rod–coil diblock copolymers.

moreover, could be efficiently manipulated by controlling the rod-to-coil block ratio. For example, the thin film morphology of P3HT-*b*-oxadiazole was influenced on the coil length of pendent oxadiazole in our previous study. As the length of oxadiazole coils increased, the poor P3HT crystalline structure was found, diminishing the p-channel charge carrier mobility.[30]

The acceptor units in the above-mentioned block copolymers (i.e., C_{60} or perylene bisimides), however, are not easy to be purified and functionalized for synthesis. Isoindigo is a structural isomer of the nature pigment indigo and can be prepared with a simple synthetic route. It provided considerable electron-withdrawing ability for high performance OFET (mobility larger than 4 $cm^2\ V^{-1}\ s^{-1}$)[37,38] and solar cells (efficiency up to 6%).[39] However, the above-mentioned isoindigo-based devices mainly used the isoindigo moiety in polymer main chain. A pendent conjugated isoindigo building block, which can be served as a coil segment in a block copolymer, has not been reported yet, to the best of our knowledge.

Herein, we report the synthesis, morphology, and properties of D–A diblock copolymer consisting of a P3HT rod and a poly(pendent isoindigo) coil segment, $P3HT_{44}$-*b*-$Piso_n$. It is the first example of using D–A rod–coil copolymer for OFET memory devices, as far as we know. The P3HT and Piso blocks were designed to be the charge transporting and storage elements for the OFET memory devices, respectively, which were without an additional charge storage layer. The P3HT and Piso blocks were prepared using the Grignard metathesis polymerization and ATRP, respectively, and then coupled via the click reaction to obtain the targeted block copolymers. Note that the block length of P3HT was fixed at 44 repeating units, and those of Piso coil were varied with 10, 20, 60, and 100 pendent isoindigo units, as shown in **Scheme 1**. The morphology of the

© 2016 WILEY-VCH Verlag GmbH & Co. KGaA, Weinheim

Table 1. Molar ratios, molecular weights and their distributions of P3HT$_{44}$, N$_3$-Piso$_n$, and P3HT$_{44}$-*b*-Piso$_n$ block copolymers.

Sample	[M]/[AHBMP][a]	$M_{n,theo}$[b]	$M_{n,SEC}$[c]	$M_{n,NMR}$[d]	M_w/M_n[c]
N$_3$-Piso$_{10}$	20	5100	3800	4700	1.18
N$_3$-Piso$_{20}$	40	10 100	7900	9900	1.13
N$_3$-Piso$_{60}$	100	30 400	21 700	30 700	1.15
N$_3$-Piso$_{100}$	150	50 200	33 200	51 200	1.22
P3HT$_{44}$	–	–	10 500	7400	1.23
P3HT$_{44}$-*b*-Piso$_{10}$	–	–	13 500	12 100	1.25
P3HT$_{44}$-*b*-Piso$_{20}$	–	–	15 300	17 300	1.21
P3HT$_{44}$-*b*-Piso$_{60}$	–	–	17 800	38 100	1.23
P3HT$_{44}$-*b*-Piso$_{100}$	–	–	28 500	58 600	1.34

[a]Standard polymerization conditions: 80 °C, [CuBr]:[PMDETA] = 1:1, concentration of monomer = 0.26 M; [b]Calculated based on the monomer conversion; [c]Determined from SEC using PSt standards in THF; [d]Determined by ^{1}H-NMR in $CDCl_3$.

prepared P3HT$_{44}$-*b*-Piso$_n$ was characterized using atomic force microscopy (AFM), grazing-incidence X-ray diffraction (GIXD), and grazing-incidence small-angle X-ray scattering (GISAXS). The OFET mobility and memory characteristics were measured using a top-contact bottom gate device configuration and correlated with the P3HT/Piso ratio and the film morphology.

2. Results and Discussion

2.1. Synthesis and Characterization of P3HT$_{44}$-*b*-Piso$_n$

Scheme 1 outlines the synthetic pathway of the methacrylate-functionalized isoindigo monomer (**5**), and the experimental details are summarized in the Supporting Information. We first established the synthetic procedure for the asymmetric isoindigo side chain, i.e., compound **4**, which was a key compound to access the desired monomer **5**. 1-(2-Ethylhexyl) indoline-2,3-dione (**1**) and 1-(4-hydroxybutyl)indolin-2-one (**2**) were prepared in a single operation from commercially available indoline-2,3-dione and oxindole, respectively. The coupling reaction of **1** and **2** was performed in a mixture of acetic acid and hydrochloric acid, yielding the acetylated compound **3**. Deprotection of the acetyl group in the presence of sodium methoxide resulted in decomposing the carbon–carbon bridged site because of a high basicity. We therefore employed sodium carbonate for the deprotection reaction and successfully obtained compound **4**. Finally, the resulting **4** was treated with methacryloyl chloride in the presence of trimethylamine, giving the desired monomer **5** in sufficient yield.[40]

The azido-terminated poly(pendent isoindigo)s (N$_3$-Piso$_n$) were synthesized by ATRP of monomer **5** in the presence of AHBMP as initiator, in which the [monomer]$_0$/[AHBMP]$_0$ ratios of 20, 40, 100, and 150 were applied to produce the polymer with different molecular weights. Figure S5 (Supporting Information) shows the ^{1}H-NMR spectra and size exclusion chromatography (SEC) traces of the obtained poly(pendent isoindigo) with the azido end group (N$_3$-Piso$_n$, n = 10, 20, 60, 100). As shown in Figure S5a (Supporting Information), the proton signal is clearly observed at 3.21 ppm (peak h) due to the azido group as the end functional group derived from azido-methylene proton. The signals of the methylene proton from the main chain and the methyl group in the side chain are observed in the ranges of 0.43–2.61 ppm (peak i). In addition, the signals at 3.42–4.11 ppm (peaks e–g), 6.49–7.42 ppm (peaks b–d), and 8.96–9.19 (peak a) are reasonably assigned to the expected chemical structure of N$_3$-Piso$_n$. The SEC traces of each N$_3$-Piso$_n$ exhibit a unimodal elution peak with the M_w/M_n value of 1.18–1.22 (Figure S5b, Supporting Information). The molecular characteristics of the obtained N$_3$-Piso$_n$s are listed in **Table 1**.

The alkynyl-terminated P3HT was synthesized by controlled Grignard Metathesis (GRIM) polymerizations and subsequently end capping with an alkynyl group, according to the reported procedure (^{1}H-NMR and SEC data are shown in Figure S6, Supporting Information). The coupling reaction of the alkynyl-terminated P3HT ($M_{n,NMR}$ = 7400 and M_w/M_n = 1.23) and N$_3$-Piso$_{20}$ ($M_{n,NMR}$ = 9900 and M_w/M_n = 1.13) was carried out by the Cu-catalyzed azido-alkyne click reaction to produce the desired block copolymer, i.e., P3HT$_{44}$-*b*-Piso$_{20}$. The SEC trace of P3HT$_{44}$-*b*-Piso$_{20}$ ($M_{n,NMR}$ = 17 300, PDI = 1.21; Figure S7b, Supporting Information) clearly demonstrated the shift in the elution peak to the high molecular-weight region in comparison with that of its precursor N$_3$-Piso$_{20}$. The ^{1}H-NMR spectra of the P3HT$_{44}$-*b*-Piso$_{20}$ in $CDCl_3$ are shown in **Figure 1**a, with the proton signals at *a* (9.19–8.96 ppm), *b* (7.39–7.13 ppm), *c* (7.08–6.83 ppm), *d* (6.83–6.57 ppm), and *e* (6.98 ppm) due to the N$_3$-Piso$_n$ aromatic protons and P3HT of the polymer main chain, *f* (4.46–4.25 ppm), *g–i* (4.22–3.28 ppm), *j* (2.90–2.67 ppm) corresponding to the methylene bridge adjacent to triazole groups, methylene protons adjacent to O or N atom and α-CH_2 of P3HT. In addition, the peaks at *k* (2.15–0.59 ppm) are attributed to thiophene $-CH_2$, main chain backbone, and alkyl side chain. The effective coupling between the azido and alkynyl groups is further confirmed by the fact that the characteristic absorption at 2098 cm^{-1} due to N$_3$-Piso$_{20}$ azido group in the Fourier transform infrared (FTIR) spectrum completely disappears after the click reaction with alkynyl-terminated P3HT (Figure 1b). Furthermore, the elemental analyses of the carbon, hydrogen, nitrogen, and sulfur contents illustrate a good agreement with the theoretical content. Similarly, **8a**, **8c**, and **8d** with respective block compositions of P3HT$_{44}$-*b*-Piso$_{10}$, P3HT$_{44}$-*b*-Piso$_{60}$, and P3HT$_{44}$-*b*-Piso$_{100}$ were also synthesized and fully characterized by SEC, FTIR, and ^{1}H NMR, as shown

© 2016 WILEY-VCH Verlag GmbH & Co. KGaA, Weinheim

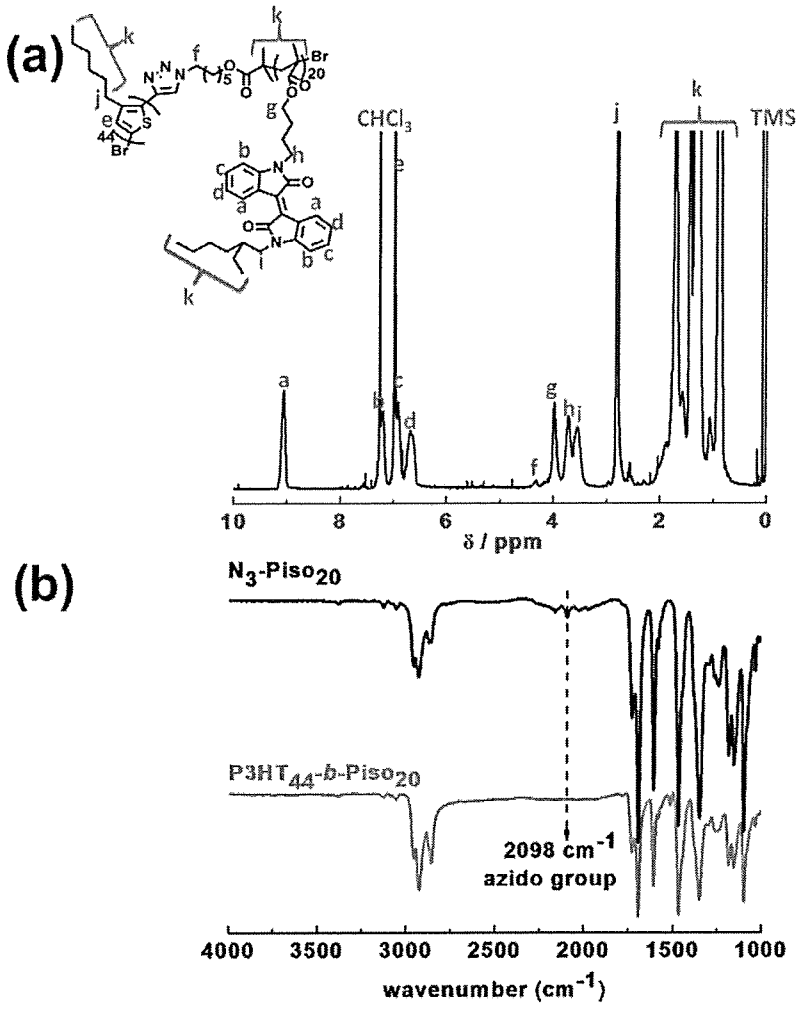

Figure 1. a) ^{1}H-NMR spectra of P3HT$_{44}$-*b*-Piso$_{20}$ in $CDCl_3$, b) IR spectra of N_3-Piso$_{20}$ and P3HT$_{44}$-*b*-Piso$_{20}$.

in Figures S8–S10 (Supporting Information). The number-averaged molecular weight and polydispersity of the prepared block copolymers are summarized in Table 1. All the synthesized polymers are easily soluble in common organic, such as o-dichlorobenzene, chloroform, tetrahydrofuran, and toluene.

2.2. Thermal Properties

The thermal characteristics of P3HT$_{44}$, N_3-Piso$_{100}$, and P3HT$_{44}$-*b*-Piso$_n$ were investigated by thermogravimetric analysis and differential scanning calorimetry (DSC), as shown in Figure S11a,b (Supporting Information), respectively. The thermal decomposition temperatures (T_d, 5% weight-loss) values of P3HT$_{44}$ and N_3-Piso$_{100}$ are 430 and 275 °C, respectively. The studied P3HT$_{44}$-*b*-Piso$_n$ block copolymers exhibit T_ds between the decomposition of P3HT and Piso domains. Note that the T_d of the studied block copolymer decreases with increase in the content of Piso due to the low thermal stability of the Piso segment. On the other hand, the DSC traces of the studied materials are shown in Figure S11b (Supporting Information). Thermal glass transition temperatures (T_g) of P3HT$_{44}$-*b*-Piso$_n$ observed at 50–80 °C are systematically enlarged as the Piso block length increased, attributed to the influence of Piso coils (i.e., with a T_g of 87 °C). In addition, the melting temperatures (T_m) peaks of P3HT$_{44}$-*b*-Piso$_n$ are observed in a range of 193–207 °C, which is dominated by the P3HT blocks. With the increase of Piso coil length, the endothermic peak becomes weaker, and the T_m is generally shifted to a lower temperature for the prepared P3HT$_{44}$-*b*-Piso$_n$ copolymers. These phenomena can be explained by the disturbed P3HT interchain packing and the further confined P3HT crystallization while the Piso block with a longer chain length would need more space for stretching.[41]

2.3. Optical and Electrochemical Properties

Figure 2a and Figure S12 (Supporting Information) present the normalized solid and solution state UV–vis absorption spectra of P3HT$_{44}$, N_3-Piso$_{100}$, and P3HT$_{44}$-*b*-Piso$_n$, and their corresponding maximum absorption wavelengths (λ_{max}) and optical band gaps (E^{opt}_g) are summarized in Table 2. The P3HT$_{44}$ and P3HT$_{44}$-*b*-Piso$_n$ block copolymers exhibit extensive structural organizing in solid state since an obvious red shift (i.e., 60–90 nm) from solution to film state is observed. The P3HT$_{44}$-*b*-Piso$_{10}$ and P3HT$_{44}$-*b*-Piso$_{20}$ thin films exhibit a clear λ_{max} at 515–520 nm with a vibrational peak at 600 nm. Such features are similar to the P3HT$_{44}$ homopolymer. It strongly suggests that the nature of Piso coils does not interrupt the inter or intra-chain packing as well as π–π stacking structures of the P3HT block, as the content of P3HT in P3HT$_{44}$-*b*-Piso$_n$ is higher than 40 wt%. On the contrary, the absorption peak wavelengths at 272 and 393 nm (i.e., the absorption of Piso coil) are stronger than the λ_{max} at 526 nm (i.e., the absorption of P3HT rod) for P3HT$_{44}$-*b*-Piso$_{60}$ and P3HT$_{44}$-*b*-Piso$_{100}$ thin films, which can be mainly attributed to the increased length of Piso segment. The corresponding E^{opt}_g of P3HT$_{44}$, N_3-Piso$_{100}$, P3HT$_{44}$-*b*-Piso$_{10}$, P3HT$_{44}$-*b*-Piso$_{20}$, P3HT$_{44}$-*b*-Piso$_{60}$, and P3HT$_{44}$-*b*-Piso$_{100}$ that were estimated from the onset of the absorption spectra are 1.89, 3.28, 1.90, 1.91, 1.93, and 1.94 eV, respectively. The E^{opt}_g values of P3HT$_{44}$-*b*-Piso$_n$ block copolymers become slightly larger as the length of Piso is increased, demonstrating that the P3HT/Piso block ratio can affect their optoelectronic properties.

The oxidation and reduction behaviors as well as the energy levels of the studied polymers were investigated using cyclic voltammetry, as shown in Figure 2b and summarized in Table 2. Spin-coated polymer films on an Indium Tin oxide

© 2016 WILEY-VCH Verlag GmbH & Co. KGaA, Weinheim

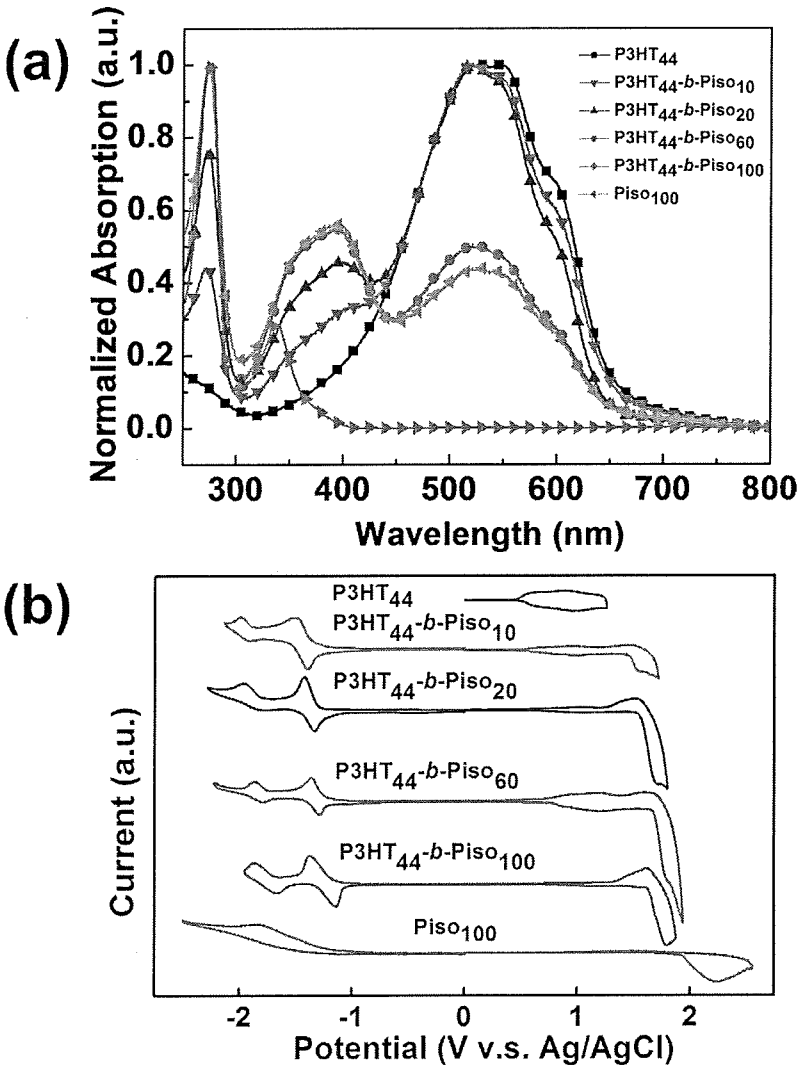

Figure 2. a) UV–vis absorption spectra as thin films cast from *o*-dichlorobenzene (10 mg mL^{-1}) solution and b) cyclic voltammetry curves of the studied materials.

(ITO)-coated glass substrate were measured in dry acetonitrile containing 0.1 M of tetrabutylammonium perchlorate as an electrolyte under nitrogen atmosphere. The highest occupied molecular orbital (HOMO) and lowest unoccupied molecular orbital (LUMO) energy levels were calculated from the onset oxidations (E_{onset}^{ox}) and onset reductions (E_{onset}^{red}) with reference to ferrocene (4.8 eV) using the equation HOMO = $-e[E_{onset}^{ox} - E_{ferrocene}^{1/2} + 4.8]$ V and LUMO = $-e[E_{onset}^{red} - E_{ferrocene}^{1/2} + 4.8]$ V. The corresponding HOMO and LUMO levels of the studied polymers are in a range of −4.81 to −6.24 and −2.92 to −3.22 eV, respectively, as listed in Table 2. From the results, the lower HOMO and LUMO energy levels of the studied P3HT$_{44}$-*b*-Piso$_n$ are observed as the increased Piso block ratio due to stronger electron affinity. Such difference on the energy level and electron-withdrawing ability would significantly affect the electrical properties, especially the charge storage memory behaviors, as discussed later.

2.4. Morphology of the P3HT$_{44}$-*b*-Piso$_n$ Thin Films

The surface structures of P3HT$_{44}$-*b*-Piso$_n$ thin films were explored using AFM. No obvious surface structure is observed on the as-cast thin films (i.e., without thermal annealing treatment) of all studied block copolymers (see Figure S13 in the Supporting Information). On the contrary, nanofibrillar-like morphology is clearly observed for the thin film after thermal annealing, as shown in **Figure 3**. For P3HT$_{44}$-*b*-Piso$_{10}$ and P3HT$_{44}$-*b*-Piso$_{20}$, the low Piso content does not significantly affect the nanofibrillar formation (P3HT) and amorphous (Piso) blocks.[42] To further investigate the relationships between P3HT/Piso ratio and the domain size of phase separation in P3HT$_{44}$-*b*-Piso$_n$ thin films, grazing-incidence small-angle X-ray scattering (GISAXS) was introduced. From the 1D-GISAXS profiles of P3HT$_{44}$-*b*-Piso$_n$ thin films after thermal annealing (Figure S14,

Table 2. Physiochemical properties of P3HT$_{44}$, N$_3$-Piso$_n$, and P3HT$_{44}$-*b*-Piso$_n$ block copolymers.

Sample	wt% of P3HT	$\lambda^{soln}{}_{max}$ [a)] [nm]	$\lambda^{film}{}_{max}$ [b)] [nm]	$E^{opt}{}_{g}$ [c)] [eV]	HOMO [eV]	LUMO [eV]	*d*-spacing [d)] [nm^{-1}]
P3HT$_{44}$	100	450	520 548	1.89	−4.81	−2.92 [e)]	–
P3HT$_{44}$-*b*-Piso$_{10}$	61.2	275 412 448	273 518 543	1.90	−4.86	−2.98	19.6
P3HT$_{44}$-*b*-Piso$_{20}$	43.3	274 447	272 517 541	1.91	−4.95	−3.03	23.2
P3HT$_{44}$-*b*-Piso$_{60}$	19.4	272 396 469	272 390 526	1.93	−5.09	−3.09	29.9
P3HT$_{44}$-*b*-Piso$_{100}$	12.6	273 394 467	273 390 529	1.94	−5.13	−3.19	39.3
N$_3$-Piso$_{100}$	0	274 374	276 342	3.28	−6.24	−3.22	–

[a)]Absorption spectra in *o*-dichlorobenzene solution; [b)]Spin-cast film from *o*-dichlorobenzene solution onto a quartz substrate; [c)]Estimated from onset wavelength (λ_{onset} (nm)) of the UV–vis absorption and using the formula $E^{opt}{}_{g} = 1240/\lambda_{onset}$ (nm); [d)]Determined by GISAXS measurement using thermal-annealed thin film samples; [e)]The LUMO energy level was estimated by the equation LUMO (eV) = HOMO + $E^{opt}{}_{g}$.

© 2016 WILEY-VCH Verlag GmbH & Co. KGaA, Weinheim

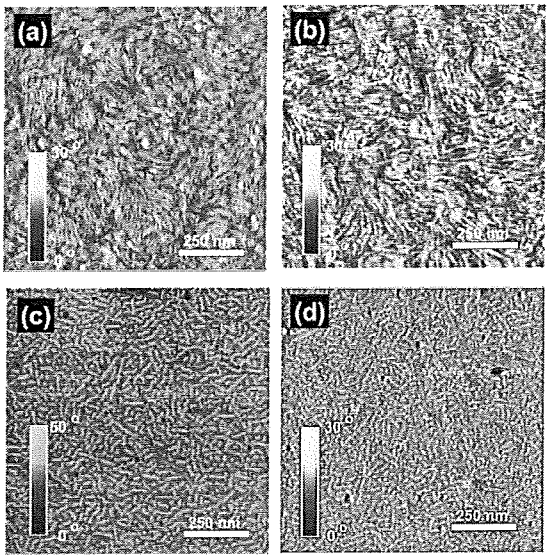

Figure 3. AFM phase images of a) $P3HT_{44}$-*b*-$Piso_{10}$, b) $P3HT_{44}$-*b*-$Piso_{20}$, c) $P3HT_{44}$-*b*-$Piso_{60}$, and d) $P3HT_{44}$-*b*-$Piso_{100}$. All the polymer films were annealed at 140 °C under vacuum for 1 h.

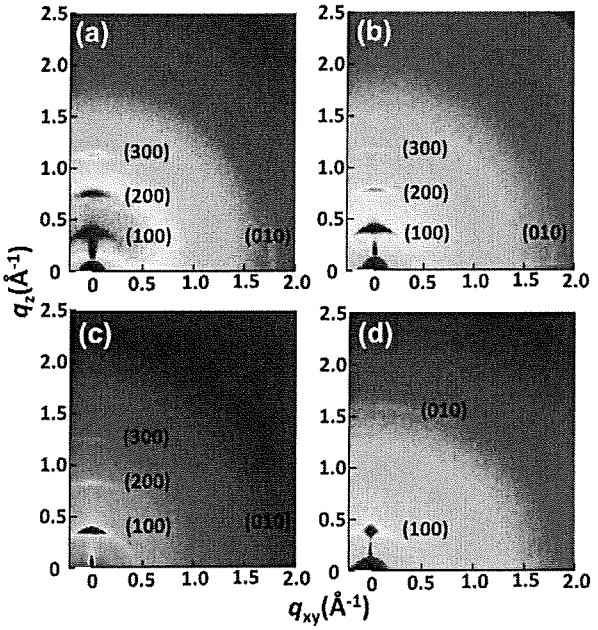

Figure 4. 2D GIXD patterns of thermal-annealed $P3HT_{44}$-*b*-$Piso_n$ thin films: a) $P3HT_{44}$-*b*-$Piso_{10}$, b) $P3HT_{44}$-*b*-$Piso_{20}$, c) $P3HT_{44}$-*b*-$Piso_{60}$, and d) $P3HT_{44}$-*b*-$Piso_{100}$.

Supporting Information), clear first-order scattering peaks at $q^* = 0.032$ ($P3HT_{44}$-*b*-$Piso_{10}$), 0.027 ($P3HT_{44}$-*b*-$Piso_{20}$), 0.021 ($P3HT_{44}$-*b*-$Piso_{60}$), and 0.016 ($P3HT_{44}$-*b*-$Piso_{100}$) Å^{-1} can be detected, respectively. The *d*-spacing (i.e., center-to-center distance) is then calculated accordingly based on the equation of $d = 2\pi/q^*$, and their corresponding *d* values are 19.6, 23.2, 29.9, and 39.3 nm, respectively. It indicates that the phase separation of the P3HT rods, leading to high density fibrillar-like nanostructures on the thin film surface. As the content of Piso is increased ($P3HT_{44}$-*b*-$Piso_{60}$ and $P3HT_{44}$-*b*-$Piso_{100}$), the surface structures become worm-like nanofibers with the lower density of P3HT large aggregate domains, which is owing to a balance between thermodynamics and kinetics between crystalline domain sizes can be controlled by tuning the block length of Piso.

Not only large-scale aggregations but also molecular packing nanostructures between polymer chains are important to analyze because it may directly affect the electrical properties of the prepared polymer thin films. The molecular packing features of $P3HT_{44}$-*b*-$Piso_n$ were collected using grazing-incidence X-ray diffraction (GIXD). **Figure 4** shows the 2D GIXD patterns of thermal-annealed $P3HT_{44}$-*b*-$Piso_n$ thin films deposited on the octadecyltrichlorosilane (ODTS) modified Si substrates, and distinguishable diffraction signals in both in-plane (q_y) and out-of-plane (q_z) directions are observed. The packing orientation distribution of crystallites, moreover, was determined from the lamella peaks (i.e., (100), (200), and (300)) and the π–π stacking peak (i.e., (010)). For $P3HT_{44}$-*b*-$Piso_{10}$, clear out-of-plane lamella signals and in-plane π–π stacking (010) diffraction can be observed (Figure 4a), indicating a relatively edge-on packing orientation and similar to that of $P3HT_{44}$ homopolymer (Figure S15, Supporting Information). Note that all the studied block copolymers exhibit a lamellar spacing of 16.3 Å and a π–π stacking distance of 3.82 Å, meaning that the packing structure is dominate by P3HT block in the polymer backbone.[43] As the Piso block length increased in the studied block copolymers, the edge-on population decreased relative to the face-on population. Note that the intensity of (010) in the in-plane direction becomes weaker at a larger block length, whereas the (010) in the out-of-plane direction becomes stronger (Figure 4d). This transition implies that the molecular packing orientation would be affected by the P3HT/Piso ratio in the polymer chain, and then influence on the charge carrier transporting in the polymer thin films. Furthermore, the intensity of lamella peaks in the out-of-plane direction is decreased with increasing the block length of Piso, indicating poorer degree of interchain packing as well as charge transport ability. For $P3HT_{44}$-*b*-$Piso_n$ with a higher content of P3HT, higher crystallinity and relatively edge-on packing orientation may provide more efficient charge transport between or inside polymer chain.

2.5. OFET Characteristics of $P3HT_{44}$-*b*-$Piso_n$

To understand the charge transporting properties of $P3HT_{44}$-*b*-$Piso_n$, OFET with the configuration of top-contact bottom gate was fabricated. The studied block copolymers were spin-coated on the ODTS-modified SiO_2/Si substrates under a nitrogen atmosphere and thermally annealed at 140 °C under vacuum for 1 h. **Figure 5**a and Figure S16 (Supporting Information) show the p-type output curves of the thermal-annealed $P3HT_{44}$-*b*-$Piso_n$ thin films, and stable current modulation as well as well-defined linear and saturation regions can be observed. Moreover, the transfer curves of 140 °C annealed $P3HT_{44}$-*b*-$Piso_n$ thin films are explored in Figure 5b. The saturation-regime mobility was calculated from the slope of the plot of drain/source current $(I_{ds})^{-0.5}$ as a function of the gate voltage

© 2016 WILEY-VCH Verlag GmbH & Co. KGaA, Weinheim

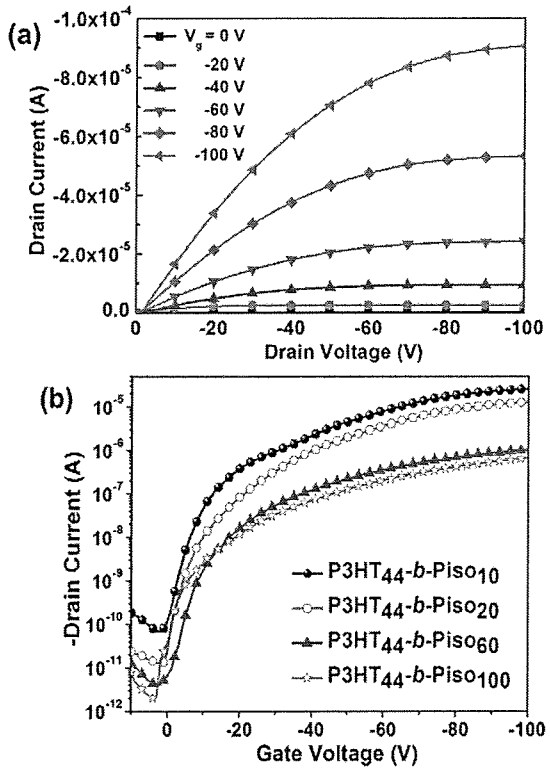

Figure 5. a) OFET output curves of P3HT$_{44}$-*b*-Piso$_{10}$ and b) transfer characteristics of P3HT$_{44}$-*b*-Piso$_n$ block copolymers. The source/drain voltage was set as −50 V.

(V_g). The correlation between the I_{ds} and other parameters is shown using the following equation[44]

$$I_{ds} = 0.5WC_i\mu L^{-1}\left(V_g - V_t\right)^2 \quad (1)$$

where I_{ds} is the drain-to-source current in the saturated region, W is the channel width, L is the channel length, μ is the hole mobility, C_i is the capacitance per unit area of the insulation layer (300 nm SiO_2, $C_i = 10$ nF cm^{-2}), and V_g and V_t are the gate and threshold voltages, respectively. The device performances including mobility (μ), on/off current ratio, and threshold voltage (V_{th}) are summarized in **Table 3**. The calculated average p-channel mobility is 0.046, 0.021, 1.62 × 10^{-3}, and 6.45 × 10^{-4} cm^2 V^{-1} s^{-1} for P3HT$_{44}$-*b*-Piso$_{10}$, P3HT$_{44}$-*b*-Piso$_{20}$, P3HT$_{44}$-*b*-Piso$_{60}$, and P3HT$_{44}$-*b*-Piso$_{100}$, respectively, with an on/off current ratio of 10^5–10^6. Note that these mobilities are 10–100 times higher than the as-cast P3HT$_{44}$-*b*-Piso$_n$ thin films, indicating that the thermal annealing process can significantly improve the charge transport ability. It is mainly attributed to the enhanced P3HT domain aggregation as well as molecular packing, as evidenced by AFM analyses. On the other hand, the charge carrier mobilities of P3HT$_{44}$-*b*-Piso$_{10}$ (0.046 cm^2 V^{-1} s^{-1}) and P3HT$_{44}$-*b*-Piso$_{20}$ (0.021 cm^2 V^{-1} s^{-1}) are similar to that of P3HT$_{44}$ homopolymer (0.041 cm^2 V^{-1} s^{-1}; Figure S18, Supporting Information). In addition, the field-effect mobility of the studied block copolymers is reduced as the Piso coil length is increased, owing to the thin film morphology, as discussed in the results of AFM, GISAXS, and GIXD. With a higher phase-separated P3HT domain density, crystallinity, and facilitated edge-on packing orientation, P3HT$_{44}$-*b*-Piso$_{10}$ possesses the highest charge carrier mobility among the series of P3HT$_{44}$-*b*-Piso$_n$.

2.6. Transistor-Type Memory Characteristics

P3HT$_{44}$-*b*-Piso$_n$ block copolymers are design to exhibit both superior charge transport and charge storage abilities. Good holes mobility (up to 0.046 cm^2 V^{-1} s^{-1}) mainly affected by the P3HT crystalline networks has been demonstrated in FET characterizations. The charge storage and memory phenomena, furthermore, were probed using the same studied P3HT$_{44}$-*b*-Piso$_n$ copolymers-based FET devices. Memory characteristics of both as-cast and thermal-annealed thin films were investigated with a programming gate pulse of ±100 V, as shown in **Figure 6** and Figures S19 and S22 (Supporting Information).

Table 3. Summary of FET and OFET memory characteristics for the P3HT$_{44}$-*b*-Piso$_n$-based devices.

Sample[a]	FET		Memory			
	μ_{avg}[b] [cm^2 V^{-1} s^{-1}]	$I_{on}/I_{off,avg}$ [–]	Memory ratio [–]	$V_{t,writing}$ [V]	$V_{t,erasing}$ [V]	ΔV_t[c] [V]
P3HT[c]	(1.4 ± 0.2) × 10^{-3}	3.8 × 10^3	–	–	–	–
P3HT[d]	(4.1 ± 0.1) × 10^{-2}	1.5 × 10^3	–	–	–	–
P3HT$_{44}$-*b*-Piso$_{10}$[d]	(7.1 ± 0.1) × 10^{-4}	1.4 × 10^4	2.4 × 10^4	15 ± 1	2 ± 1	13 ± 3
P3HT$_{44}$-*b*-Piso$_{10}$[e]	(4.6 ± 0.1) × 10^{-2}	3.8 × 10^5	3.1 × 10^5	20 ± 1	−6 ± 1	26 ± 3
P3HT$_{44}$-*b*-Piso$_{20}$[d]	(3.1 ± 0.2) × 10^{-4}	3.7 × 10^4	4.7 × 10^4	18 ± 2	−3 ± 1	21 ± 2
P3HT$_{44}$-*b*-Piso$_{20}$[e]	(2.1 ± 0.1) × 10^{-2}	1.3 × 10^6	3.3 × 10^6	32 ± 2	−17 ± 2	49 ± 2
P3HT$_{44}$-*b*-Piso$_{60}$[d]	(8.9 ± 0.3) × 10^{-5}	4.1 × 10^3	7.1 × 10^3	36 ± 1	2 ± 1	34 ± 3
P3HT$_{44}$-*b*-Piso$_{60}$[e]	(1.6 ± 0.2) × 10^{-3}	2.6 × 10^5	4.9 × 10^5	51 ± 1	−11 ± 1	62 ± 4
P3HT$_{44}$-*b*-Piso$_{100}$[d]	(2.7 ± 0.3) × 10^{-5}	5.2 × 10^3	3.7 × 10^3	41 ± 1	1 ± 1	42 ± 2
P3HT$_{44}$-*b*-Piso$_{100}$[e]	(6.5 ± 0.1) × 10^{-4}	3.2 × 10^5	4.3 × 10^5	71 ± 1	−8 ± 1	79 ± 3

[a]All the electrical properties were averaged from at least 15 devices of three different batches; [b]Mobility calculated from saturation region and calibrated with the capacitance of polymer eletrects; [c]ΔV_t is defined as $V_{t,writing} - V_{t,erasing}$; [d]As-cast thin films; [e]Thermal-annealed thin films.

© 2016 WILEY-VCH Verlag GmbH & Co. KGaA, Weinheim

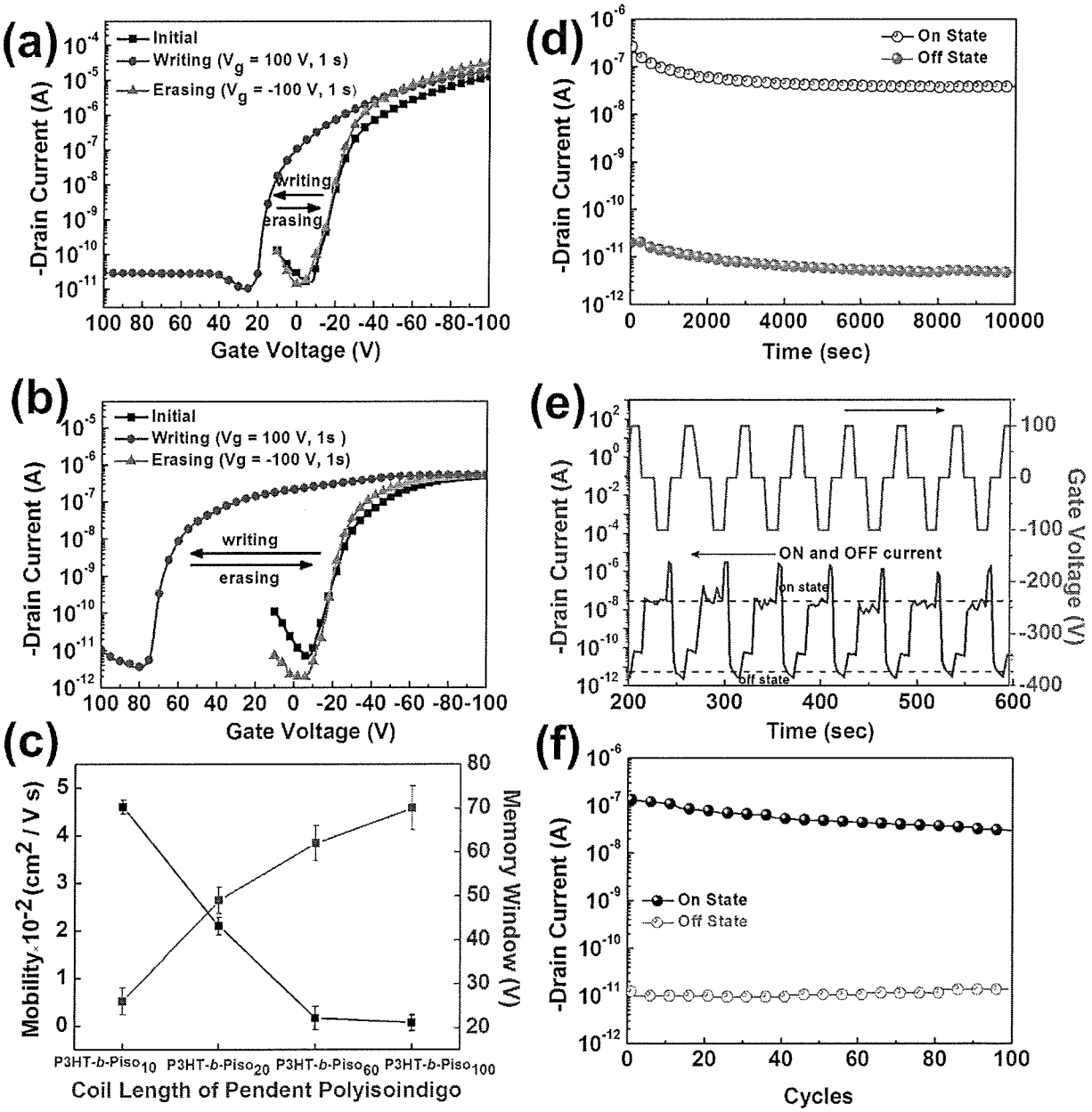

Figure 6. Electrical properties of a) $P3HT_{44}$-*b*-$Piso_{10}$ and b) $P3HT_{44}$-*b*-$Piso_{100}$-based FET memory device, where $V_g = 100$ V and $V_g = -100$ V were applied around 1 s for writing and erasing, respectively. c) The averaged FET mobility and memory window of thermal-annealed $P3HT_{44}$-*b*-$Piso_n$ thin films as a function of Piso coil length. d) Retention times of the ON and OFF states, e) reversible current response to the WRER cycles, and f) endurance of WRER cycles of the $P3HT_{44}$-*b*-$Piso_{20}$-based FET memory device.

Also, the detailed memory behaviors are summarized in Table 3. Note that the high operation voltage in this study is restricted by low capacitance of SiO_2 dielectric layer. All four studied block copolymers exhibit similar memory switching characteristics that when applying a positive gate bias (V_g = 100 V, V_d = 0 V for 1 s), the original transfer curves (i.e., initial state) are substantially shifted toward the positive voltage direction, as defined to as the "writing process." This shift results in a high source-to-drain current level (i.e., ON state) at V_g = 0 V. On the contrary, the transfer curves are shifted reversely and back to the initial state when applying a negative gate bias ($V_g = -100$ V, V_d = 0 V for 1 s), referring to as the "erasing" process. Indeed, the shifting changes between the transfer curve after giving writing and subsequently an erasing gate bias is defined as the memory windows (ΔV_{th}).

The $P3HT_{44}$ homopolymer is employed as the reference device (see Figure S18 in the Supporting Information) for comparison. Only a negligible threshold voltage shift could be

© 2016 WILEY-VCH Verlag GmbH & Co. KGaA, Weinheim

detected for such polymer without pendent isoindigo moieties. However, the FET memory based on P3HT$_{44}$-*b*-Piso$_{10}$, P3HT$_{44}$-*b*-Piso$_{20}$, P3HT$_{44}$-*b*-Piso$_{60}$, and P3HT$_{44}$-*b*-Piso$_{100}$ exhibits the memory windows of 13, 21, 34, and 42 V for the as-cast device, and 26, 49, 62, and 79 V for the thermal-annealed device. A significant enhancement (approximately two times) of memory window can be explored for the FET memories after thermal treatment, leading to a more efficient charge storage (i.e., electron trapping) in the memory cell. The thermal annealing process can effectively generate the good phase separation and form a more stable aggregate or packing morphology of the P3HT (donor) and Piso (acceptor) domains, preventing charge recombination in the channel of P3HT. Thus, the electrons can be trapped effectively and remain in Piso domain, resulting in an improved memory window. Since the positive-gate-induced electrons are delocalized and stabilized within pendent isoindigo acceptors with an extremely low conjugated length, the larger memory window of the FET memory device with the longer length of the Piso segments can be observed. However, as the copolymer contains a higher ratio of the Piso block (i.e., lower content of P3HT), the field-effect mobility becomes poorer. Figure 6c concludes the trends of mobility and memory window for the P3HT$_{44}$-*b*-Piso$_n$ copolymers, the FET and FET memory properties can be directly manipulated through the molecular design. Among them, P3HT$_{44}$-*b*-Piso$_{20}$ possesses appropriate memory window and relatively high mobility, which can be served as an emerging material for high performance FET memory devices. It is worth to note the highest charge storage density (0.4) of the studied block polymers (P3HT$_{44}$-*b*-Piso$_{100}$), which were calculated by the memory window divide by summarizing the writing and erasing voltage. These are comparable to that of the high-performance polymer-electret-based transistor memories with a bilayer device configuration (evaporated semiconducting molecules/polymer heterostructure) which reported the charge storage density around 0.3–0.5 previously.[15,45]

The stability endurances of P3HT$_{44}$-*b*-Piso$_{20}$-based memory device are depicted in Figure 6d–f. Detailed stability results for other devices with or without annealing are summarized in the Supporting Information. The retention time of the ON and OFF states of the P3HT$_{44}$-*b*-Piso$_{20}$-based device at $V_g = 0$ V is maintained for at least 10^4 s with the I_{ON}/I_{OFF} ratios above 10^4 (Figure 6d). The ON/OFF state switching stability of such device, moreover, was evaluated based on write–read–erase–read (WRER) cycle measurements (Figure 6e). The WRER cycles were measured as follows: the drain current was kept at $V_d = -100$ V, and the writing, reading, and erasing processes were implemented at $V_g = -100$, 0, and 100 V, respectively. The results in Figure 6f demonstrate that the memory device using P3HT$_{44}$-*b*-Piso$_{20}$ as the electret could achieve a memory ratio around 10^4 over 100 cycles. Note that a poor retention characteristic was probed for P3HT$_{44}$-*b*-Piso$_{10}$-based memory device due to the highest conjugated P3HT concentration with the low degree of phase separation of polymer thin film. Thus, the delocalized electrons on isoindigo moieties are easily to recombine with the mobile holes of P3HT domain. Devices based on other copolymers, otherwise, excellent operating stability and reversibility are illustrated, as shown in Figure 6 and Figures S20, S21, and S23 (Supporting Information). In addition, the air stability was obviously affected by the addition of Piso blocks, due to the deeper HOMO level compared with that of the parent P3HT. With the longer length of the Piso segment, the better stability of the device is exhibited and possesses higher on/off current ratio, as shown in Figure S24 (Supporting Information).These results demonstrate that our newly designed P3HT$_{44}$-*b*-Piso$_n$ block polymers have great potential for nonvolatile transistor-type memory applications.

2.7. Proposed Mechanism for P3HT$_{44}$-*b*-Piso$_n$-Based Memory Device

The illustrated energy level diagram and proposed mechanism of P3HT$_{44}$-*b*-Piso$_n$-based memory device are depicted in **Figure 7**. The LUMO energy levels of P3HT and Piso are −2.92 and −3.22 eV, respectively. During the writing process, a large number of electrons are induced at the LUMO level of Piso by the positive electric field, leading to a positive V_{th}

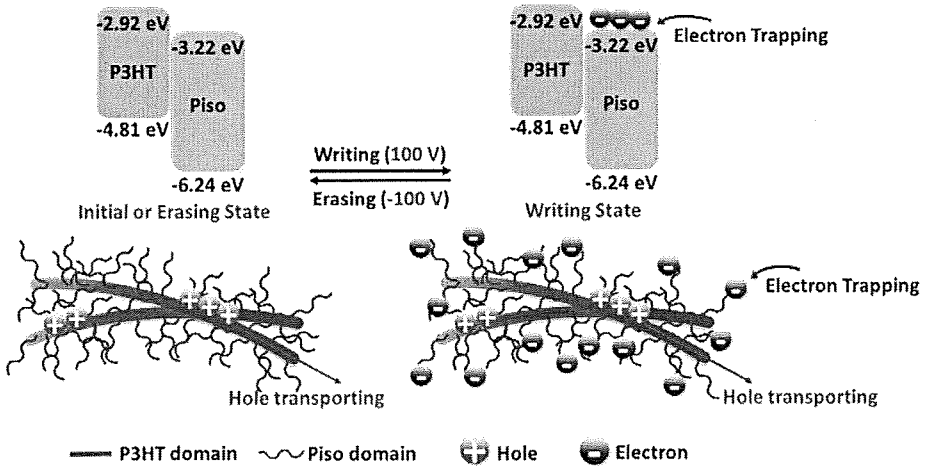

Figure 7. Illustration of energy levels of P3HT rod and Piso coil and the proposed mechanism of P3HT$_{44}$-*b*-Piso$_n$ memory device under a voltage bias.

© 2016 WILEY-VCH Verlag GmbH & Co. KGaA, Weinheim

shift because the generated electrons in Piso domain would then induce extra holes accumulated in the P3HT channel before scanning. On the contrary, the trapped electrons at Piso coil can be erased using a negative voltage bias, and the V_{th} is shifted back to its initial state. Both hole-transporting ability and electron-trapping capability of P3HT-*b*-Piso$_n$, moreover, are highly related to the Piso coil length. As the length of Piso segment is short (i.e., P3HT$_{44}$-*b*-Piso$_{10}$), the hole carrier can pass through a highly crystalline P3HT channel with a good mobility, and only few amount of electrons can be trapped in the Piso domain, resulting in poor charge storage retention stability. On the contrary, the P3HT crystallinity as well as charge transport network is destroyed when the length of Piso coil becomes much longer (i.e., P3HT$_{44}$-*b*-Piso$_{100}$). Large amount of electrons, however, is trapped in this semiconducting thin film because of the high percentage of isoindigo moiety and low-lying LUMO level, leading to a large memory window.

3. Conclusion

In summary, we have successfully prepared new rod–coil diblock copolymers P3HT-*block*-poly(pendent isoindigo) (Piso), with both charge transporting and storage characteristics for high performance transistor memory applications. The synthesized pendent isoindigo homopolymers (Piso) with different length varying from 10 to 100 repeating unit exhibited excellent electron withdrawing ability. After click with P3HT rod, the P3HT$_{44}$-*b*-Piso$_n$ rod–coil diblock copolymers showed distinct domains for the hole carrier transport (i.e., P3HT donor) and electron trapping (Piso acceptor). Thin films fabricated from P3HT$_{44}$-*b*-Piso$_n$ possessed nanofibrillar-like morphologies after thermal annealing, leading to superior electrical properties, as confirmed by AFM and X-ray diffraction analyses. Such P3HT$_{44}$-*b*-Piso$_n$s were then introduced as both charge transporting and charge storage layer in an OFET memory device configuration. P-type mobility up to 4.56×10^{-2} cm^2 V^{-1} s^{-1} was observed (P3HT$_{44}$-*b*-Piso$_{10}$) with an on/off ratio over 10^5, and tunable memory window in a range of 26–79 V was obtained by varying the block length of Piso coil. Stable data retention and endurance ability was shown using long-term stability test and WRER cycle as the Piso block length larger than 20. Indeed, high-performance OFET memory device could be integrated by a single semiconducting material with both charge transport and storage functions. Our results demonstrated a facile design of donor–acceptor diblock copolymers with both good hole mobility and electron affinity, and could be employed as a new device configuration for OFET memories.

4. Experimental Section

General Procedure for ATRPs in the Synthesis of Azido-Terminated Poly(pendent isoindigo) Homopolymer (6): The synthetic scheme for azido-terminated poly(pendent isoindigo) (N$_3$-Piso$_n$) is shown in Scheme 1. A typical procedure is as follows: CuBr and **5** were evacuated for 30 min in a Schlenk flask and backfilled with argon. The anhydrous anisole, PMDETA, and AHBMP initiator were degassed by three freeze-pump-thaw cycles; the liquid mixture was transferred to the other flask including monomer and CuBr. The mixture was stirred for 5 min in order to fully solute monomer. The polymerization was performed in a preheated oil bath at 80 °C and the monomer conversion was monitored by ^{1}H NMR at different polymerization time interval. The polymerization was terminated by bubbling air into the solution. The mixture was passed through a neutral Al_2O_3 column and eluted with tetrahydrofuran (THF) to remove the catalyst. The deep red filtrate was concentrated under reduced pressure and slowly dripped into methanol (keeping temperature around 10–15 °C). After stirring for 10 min, the red solid precipitate was collected by filtration and dried under vacuum.

General Procedure for Click Reactions in the Synthesis of P3HT$_{44}$-b-Piso Diblock Comopolymer (8): Click reaction between alkynyl-terminated P3HT and azido-terminated Piso was performed according to Scheme 1. A typical procedure is as follows: N$_3$-Piso$_n$, P3HT$_{44}$, and CuBr were placed in a Schlenk flask. The flask was evacuated 1 h and then backfilled with argon. Anhydrous THF and PMDETA were degassed by three freeze-pump-thaw cycles; the liquid mixture was transferred to the other flask including P3HT$_{44}$, N$_3$-Piso$_n$ homopolymers, and CuBr. The sealed reaction flask was stirred for 24 h at room temperature. To monitor the ^{1} H-NMR, FTIR and SEC in order to check the click reaction were finished and terminated. The polymer solution was purified over a short pad of neutral Al_2O_3 column to remove the copper catalyst. The deep purple filtrate was concentrated under reduced pressure and slowly dripped into methanol (keeping temperature around 0–5 °C). The dark purple solid was collected by filtration and dried under vacuum.

Fabrication and Characterization of Field-Effect Transistor and Memory Devices: The FETs were fabricated using the studied copolymers with a top-contact configuration. A 300 nm SiO_2 layer (capacitance per unit area = 10 nF cm^{-2}) as a gate dielectric was thermally grown onto the highly n-type doped Si (100) substrates. A silane coupling agent, ODTS, was used to modify SiO_2 layer using the following preparation procedure: the cleaned wafers were immersed in a 10×10^{-3} M solution of ODTS in anhydrous toluene at room temperature overnight, then the substrates were rinsed with toluene, acetone, and isopropyl alcohol, and dried with a stream of nitrogen. The studied polymers (i.e., P3HT$_{44}$-*b*-Piso$_{10}$, P3HT$_{44}$-*b*-Piso$_{20}$, P3HT$_{44}$-*b*-Piso$_{60}$, and P3HT$_{44}$-*b*-Piso$_{100}$) were first dissolved in *o*-dichlorobenzene (10 mg mL^{-1}) at 100 °C for at least 5 h, and then the polymer solutions were filtered through 0.22 μm pore size poly(tetrafluorethylene) (PTFE) membrane syringe filters. Afterward, polymer thin films (≈60 nm) were deposited on ODTS-modified SiO_2/Si substrates by the spin-coating method at a spin rate of 1000 rpm for 60 s. In addition, an annealing process (140 °C under nitrogen atmosphere for 2 h) was introduced to induce the molecular packing structures and enhance the FET performance. 70 nm thick gold source and drain contacts were subsequently thermal evaporated through a regular shadow mask, and the channel length (L) and width (W) were 50 and 1000 μm, respectively. The current–voltage characteristics of the devices were measured by using a Keithley 4200-SCS semiconductor parameter analyzer (Keithley Instruments Inc., Cleveland, OH) in a N_2-filled glovebox.

Supporting Information

Supporting Information is available from the Wiley Online Library or from the author.

Acknowledgements

The authors highly appreciate the financial support from the Ministry of Science and Technology of Taiwan. The authors also acknowledge NSRRC, Taiwan, for facilitating the X-ray experiments.

Received: November 18, 2015
Revised: December 22, 2015
Published online: March 8, 2016

© 2016 WILEY-VCH Verlag GmbH & Co. KGaA, Weinheim

[1] A. C. Arias, J. D. MacKenzie, I. McCulloch, J. Rivnay, A. Salleo, *Chem. Rev.* **2010**, *110*, 3.
[2] A. N. Sokolov, B. C. K. Tee, C. J. Bettinger, J. B.-H. Tok, Z. Bao, *Acc. Chem. Res.* **2011**, *45*, 361.
[3] H. Sirringhaus, *Adv. Mater.* **2014**, *26*, 1319.
[4] A. J. Heeger, *Adv. Mater.* **2014**, *26*, 10.
[5] A. Facchetti, *Mater. Today* **2007**, *10*, 28.
[6] Q. D. Ling, D. J. Liaw, C. Zhu, D. S. H. Chan, E. T. Kang, K. G. Neoh, *Prog. Polym. Sci.* **2008**, *33*, 917.
[7] Y.-H. Chou, H.-C. Chang, C.-L. Liu, W.-C. Chen, *Polym. Chem.* **2015**, *6*, 341.
[8] P. Heremans, G. H. Gelinck, R. Müller, K. J. Baeg, D. Y. Kim, Y. Y. Noh, *Chem. Mater.* **2011**, *23*, 341.
[9] K. J. Baeg, Y. Y. Noh, J. Ghim, S. J. Kang, H. Lee, D. Y. Kim, *Adv. Mater.* **2006**, *18*, 3179.
[10] C. Huang, J. E. West, H. E. Katz, *Adv. Funct. Mater.* **2007**, *17*, 142.
[11] K. J. Baeg, Y. Y. Noh, J. Ghim, B. Lim, D. Y. Kim, *Adv. Funct. Mater.* **2008**, *18*, 3678.
[12] Y. Guo, C.-a. Di, S. Ye, X. Sun, J. Zheng, Y. Wen, W. Wu, G. Yu, Y. Liu, *Adv. Mater.* **2009**, *21*, 1954.
[13] J.-C. Hsu, W.-Y. Lee, H.-C. Wu, K. Sugiyama, A. Hirao, W.-C. Chen, *J. Mater. Chem.* **2012**, *22*, 5820.
[14] Y.-C. Chiu, H.-S. Sun, W.-Y. Lee, S. Halila, R. Borsali, W.-C. Chen, *Adv. Mater.* **2015**, *27*, 6257.
[15] Y.-C. Chiu, C.-L. Liu, W.-Y. Lee, Y. Chen, T. Kakuchi, W.-C. Chen, *NPG Asia Mater.* **2013**, *5*, e35.
[16] H.-S. Sun, Y.-C. Chiu, W.-Y. Lee, Y. Chen, A. Hirao, T. Satoh, T. Kakuchi, W.-C. Chen, *Macromolecules* **2015**, *48*, 3907.
[17] S. T. Han, Y. Zhou, Z. X. Xu, L. B. Huang, X. B. Yang, V. A. L. Roy, *Adv. Mater.* **2012**, *24*, 3556.
[18] Y. S. Park, J. S. Lee, *Adv. Mater.* **2015**, *27*, 706.
[19] M. Kang, K. J. Baeg, D. Khim, Y. Y. Noh, D. Y. Kim, *Adv. Funct. Mater.* **2013**, *23*, 3482.
[20] J. H. Jung, S. Kim, H. Kim, J. Park, J. H. Oh, *Small* **2015**, *11*, 4976.
[21] Y. Zhou, S. T. Han, Z. X. Xu, V. A. L. Roy, *Adv. Mater.* **2012**, *24*, 1247.
[22] C.-C. Shih, Y.-C. Chiu, W.-Y. Lee, J.-Y. Chen, W.-C. Chen, *Adv. Funct. Mater.* **2015**, *25*, 1511.
[23] M. Sommer, A. S. Lang, M. Thelakkat, *Angew. Chem. Int. Ed.* **2008**, *47*, 7901.
[24] S. Rajaram, P. B. Armstrong, B. J. Kim, J. M. J. Fréchet, *Chem. Mater.* **2009**, *21*, 1775.
[25] S. Huettner, M. Sommer, J. Hodgkiss, P. Kohn, T. Thurn-Albrecht, R. H. Friend, U. Steiner, M. Thelakkat, *ACS Nano* **2011**, *5*, 3506.
[26] J.-H. Tsai, Y.-C. Lai, T. Higashihara, C.-J. Lin, M. Ueda, W.-C. Chen, *Macromolecules* **2010**, *43*, 6085.
[27] Y.-C. Lai, T. Higashihara, J.-C. Hsu, M. Ueda, W.-C. Chen, *Sol. Energy Mater. Sol. Cells* **2012**, *97*, 164.
[28] F. Richard, C. Brochon, N. Leclerc, D. Eckhardt, T. Heiser, G. Hadziioannou, *Macromol. Rapid Commun.* **2008**, *29*, 885.
[29] C. Yang, J. K. Lee, A. J. Heeger, F. Wudl, *J. Mater. Chem.* **2009**, *19*, 5416.
[30] Y.-K. Fang, C.-L. Liu, C. Li, C.-J. Lin, R. Mezzenga, W.-C. Chen, *Adv. Funct. Mater.* **2010**, *20*, 3012.
[31] J. Liu, E. Sheina, T. Kowalewski, R. D. McCullough, *Angew. Chem. Int. Ed.* **2002**, *41*, 329.
[32] G. Sauve, R. D. McCullough, *Adv. Mater.* **2007**, *19*, 1822.
[33] C. A. Dai, W. C. Yen, Y. H. Lee, C. C. Ho, W. F. Su, *J. Am. Chem. Soc.* **2007**, *129*, 11036.
[34] T. Higashihara, M. Ueda, *Macromolecules* **2009**, *42*, 8794.
[35] M. Urien, H. Erothu, E. Cloutet, R. C. Hiorns, L. Vignau, H. Cramail, *Macromolecules* **2008**, *41*, 7033.
[36] Y. Tao, B. McCulloch, S. Kim, R. A. Segalman, *Soft Matter* **2009**, *5*, 4219.
[37] J. Mei, K. R. Graham, R. Stalder, J. R. Reynolds, *Org. Lett.* **2010**, *12*, 660.
[38] J. Mei, H.-C. Wu, Y. Diao, A. Appleton, H. Wang, Y. Zhou, W.-Y. Lee, T. Kurosawa, W.-C. Chen, Z. Bao, *Adv. Funct. Mater.* **2015**, *25*, 3455.
[39] C.-C. Chueh, C. Z. Li, A. K.-Y. Jen, *Energy Environ. Sci.* **2015**, *8*, 1160.
[40] J. Kim, J. You, E. Kim, *Macromolecules* **2010**, *43*, 2322.
[41] J.-Y. Lee, C.-J. Lin, C.-T. Lo, J.-C. Tasi, W.-C. Chen, *Macromolecules* **2013**, *46*, 3005.
[42] X. Yu, K. Xiao, J. Chen, N. V. Lavrik, K. Hong, B. G. Sumpter, D. B. Geohegan, *ACS Nano* **2011**, *5*, 3559.
[43] R. H. Lohwasser, M. Thelakkat, *Macromolecules* **2011**, *44*, 3388.
[44] Z. Bao, J. Locklin, *Organic Field-Effect Transistors*, CRC Press, Boca Raton, FL, USA **2007**.
[45] Y.-C. Chiu, I. Otsuka, S. Halila, R. Borsali, W.-C. Chen, *Adv. Funct. Mater.* **2014**, *24*, 4240.

© 2016 WILEY-VCH Verlag GmbH & Co. KGaA, Weinheim